Mask Topography Simulation for EUV Lithography

Ron L. Gordon, Chris A. Mack

FINLE Technologies, Inc., PO Box 162712, Austin, TX 78716

Email: Ron_Gordon@finle.com

ABSTRACT

This paper introduces a methodology for rigorous computation of electric fields in the neighborhood of reflective masks employed in EUV lithography. Specifically, the media used in this application place stringent requirements on the spatial and temporal grids in order to achieve a stable and accurate Finite-Difference, Time-Domain calculation. An analytical expression for the electric field reflectivity off the multilayer is harnessed to define effective media that can decrease run times by as much as an order of magnitude. This framework is then used to analyze the effect of the absorber thickness on image linewidth and quality.

Keywords: EUV lithography, mask topography simulation, electromagnetic simulation.

1. Introduction

With the potential for sub-100 nm linewidths over a 1 μm focal range, extreme ultraviolet lithography (EUVL) holds much promise as a potential next-generation lithography. Although many difficulties loom, EUVL remains a top contender in the race to succeed optical lithography as the method of choice for manufacturing future integrated circuits.

As long as EUVL has been investigated as a viable technology, simulation of this process has been similarly researched. Although the imaging system employs Köhler illumination and, from a wave optics point of view, is very similar to optical lithography[1], there are some important differences. These differences emerge from the reflective nature of the masks and the very small wavelength of the radiation source. One of the primary modeling challenges for EUVL is therefore analyzing the topography of the masks and its effects on lithographic quantities of interest.

Mask topography analysis for EUVL is not a new concept. Such work has been performed by Nyugen, *et al.*[2], and more recently by Pistor, *et al.*[3], and Bollepalli, *et al.*[4] The works by Nyugen, *et al.,* and Pistor, *et al.,* employ a Finite-Difference, Time-Domain (FDTD) model of the EUV layout. In Nyugen, *et al.*, the issues of relative accuracy and results using different absorber materials and thicknesses are discussed. Pistor, *et al.*, on the other hand, discuss potential time-saving methods such as corner-only simulation and simulating the effect of the multilayer medium with an effective boundary condition.

We wish to introduce a computing paradigm for EUV mask topography analysis and, using the 2D FDTD mask topography simulator ProMAX/2D[5] together with the aerial image simulator in PROLITH/2, illustrate an application of it to an important issue in EUV mask making. In Section 2, we briefly analyze the accuracy and stability issues that arise here and assess their impact on our ability to provide a reliable, robust electromagnetic field simulation. Typically, the nature of the materials used here drive the allowable step sizes below a tolerable level and, like Pistor, *et al.,* we seek an alternative. Our method of attack, however, employs the analytical reflection coefficients and uses effective materials rather than effective boundary conditions; it is discussed in detail in Section 3. These analytical expressions, along with the newly obtained

results, are employed in Section 4 in a useful application of rigorous simulation methods: finding the absorber thickness that minimizes spurious reflections, and therefore aerial image sidelobes.

2. Numerical Issues

Before analyzing the problem of setting up a discrete approximation to the EUV mask, it is worth reviewing its structure and relevant parameters. A schematic of an EUV mask is shown in Figure 1. The mask consists of a good absorber of light sitting atop a substrate, which is a periodic multilayer thin film stack. The absorber is typically a metal like chrome, gold, or germanium[6], and it is not obvious how we should choose the thickness. The multilayer stack is typically composed of the combination Mo/Si or Be/Si. In the configurations of interest here – but not always – the reflectivity off the stack increases with the number of periods until it eventually reaches a limiting value. The thickness of a period is close to (but not exactly) half the wavelength of the incident radiation. The EUV radiation is incident on the mask at a shallow angle.

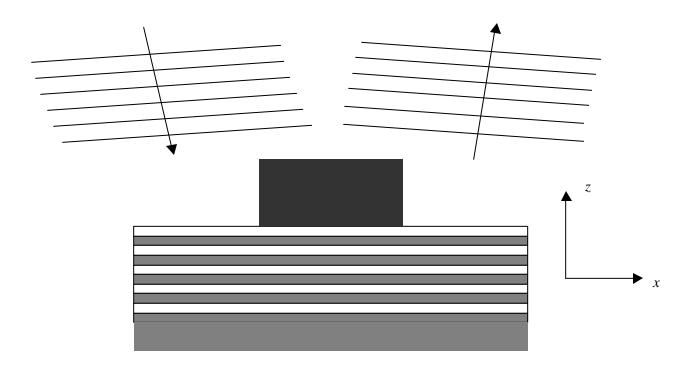**Figure 1.** Schematic of a typical EUV mask.

The parameters associated with the EUV mask, and the values used throughout this paper, are summarized in Table 1 below. We will assume a mask consisting of a chrome absorber and a Mo/Si multilayer below. Note that we have not specified the chrome absorber thickness yet; the criterion by which we will choose this thickness will be discussed in Section 4.

Parameter	Symbol	Value
Radiation wavelength	l	13.4 nm
Angle of incidence	q	4 deg
Absorber index of refraction[7]	n_{Cr}	0.933294+i 0.038224
Absorber thickness	h_{Cr}	variable
Absorber width	w	500 nm
Mo index of refraction[7]	n_{Mo}	0.922672+i 0.0062296
Mo thickness	h_{Mo}	2.08 nm
Si index of refraction[7]	n_{Si}	0.999908+i 0.00182
Si thickness	h_{Si}	4.72 nm
Background index of refraction	n_{Inc}	1.00
Substrate index of refraction	n_{Sub}	0.999908+i 0.00182
Number of periods	N	30

Table 1. Parameters used throughout the paper.

We begin to explore the numerics by studying the simplest case: that of a simple multilayer without the chrome absorbers. The problem is then reduced to one spatial dimension and the time, and the finite-difference grid becomes rather simple to lay out. Accuracy requirements will determine the size of the spatial grid cell, while stability concerns drive the size of the temporal grid cell. The discrete version of Maxwell's equations are then analyzed and updated at every time step until convergence is achieved.

The first concern we have then is accuracy as a function of spatial grid step, or, more simply, the maximum spatial step allowed to achieve a specified level of accuracy. An illustration of how an insufficient step size can affect the reflectivity results is shown in Figure 2. Here, the scattered field intensity is plotted as a function of z, the height above the multilayer. The multilayer and substrate occupy the space $z < 0$, and the space $z > 0$ is the vacuum from which the radiation is incident. In this latter region, we expect to see a straight line corresponding to the squared modulus of the reflection coefficient of the multilayer. Although simulation of a DUV transmission mask may get satisfactory results with step sizes as high as $\Delta z / l \approx 0.08$, it is clear that the choice $\Delta z / l \approx 0.03$ is extremely poor for the EUV case. In fact, a step size of $\Delta z / l \approx 0.01$ for an accuracy to within a few percent.
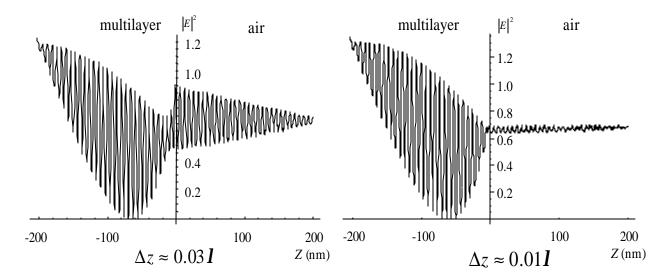
Figure 2. Scattered field intensity calculations illustrating the sensitivity of the accuracy of the FDTD computation with spatial step size. The plots above represent a multilayer reflectivity calculation with different step sizes and parameters given in Table 1.

The small spatial step size requirement, however, is only a part of the problem. The simulation must also be stable, lest small roundoff errors eventually swamp the "good" solution after enough time steps. In a lossless medium, the maximum allowable time step for a stable simulation is given by the well-known Courant condition[8]

$$\Delta t \leq \Delta z \,, \tag{1}$$

where t is the time scaled to the speed of light in vacuo $(= ct)$ and has units of distance. Therefore, at best, the maximum time step can only be as large as the spatial step we are using.

To make matters worse, the Courant time step is too large for stable calculations in the presence of our EUV multilayer stack. It turns out that sufficiently lossy materials can cause instabilities in standard FDTD schemes, independent of the time step used. We can see what happens when the material has the property $\mathrm{Re}\, n^2 < 0$ (i.e., the extinction coefficient is larger than the real part of the index of refraction): the Maxwell equations are equivalent to a wave equation of the form

$$\frac{\partial^2 E}{\partial z^2} - n^2 \frac{\partial^2 E}{\partial t^2} = 0 \,, \tag{2}$$

where the field E satisfies an initial boundary condition, and propagates indefinitely over time. This type of problem, known as the Cauchy problem, has a unique, stable solution when Eq. (2) is hyperbolic, i.e., when $\mathrm{Re}\, n^2 \geq 0$. On the other hand, when this condition is violated, Eq. (2) becomes elliptic, and the unbounded Cauchy problem leads to an unstable solution[9].

There are other materials that cause instabilties and it turns out that the actual material stability condition takes the form

$$\mathrm{Re}\, n^2 \geq 1 \,. \tag{3}$$

That is, when Eq. (3) is violated, then the computation will be unstable. The origin of the condition in Eq. (3) lies in the presence of lossless materials in the grid whose maximum time step is given by Eq. (1)[10], and its complete derivation lies beyond the scope of this paper.

What happens when Eq. (2) is violated, as is the case with the EUV multilayer materials? Wong suggested adapting an algorithm due to Leubbers for modeling frequency-dependent materials in a FDTD grid[11]. While this can lead to good results, the authors are not aware of any stability analyses that have been done for this algorithm. One of the authors (RLG), however, has implemented a different, but related, algorithm on which stability analysis is relatively straightforward[10]. Again, the details are beyond the scope of this paper, but the bottom line is that, in most cases, the maximum time step is reduced somewhat from that allowed from the Courant condition. For the EUV materials, the molybdenum is the cause of a very stringent requirement for stability: $\Delta t \leq 0.0102$ nm $< \Delta z / 10$.

3. Effective Medium Approach

With such an oppressive grid necessary for acceptable accuracy and basic stability, one begins to wonder if there is a workaround, or even if FDTD is a viable general method for simulating EUV mask topography. One workaround has been discussed by Pistor, *et al.*[3] , in the form of altered boundary conditions below the absorber layer

We take a somewhat different approach. The main assumption made here is that we are only interested in the field reflected off the mask, and not the field inside the multilayer. If the electric field reflectivity of the multilayer is known offhand, we could then search for different materials that would give the same value of this reflectivity. We would choose materials that permit us to increase the allowable time step for stability, while also keeping a similar level of accuracy. Note that such approaches as this will only work if the multilayer to be modeled is defect-free.

To begin, we need to have an independent means to compute the reflectivity off the multilayer. A simple recursive method for computing field quantities in and near thin film stacks was derived by one of the authors[12]. Nevertheless, because we are dealing with a periodic stack, a closed-form expression exists for the electric field reflectivity. Such an expression is obtained by using standard matrix methods and its derivation is presented in the Appendix. We then have a means of computing the complex electric field reflectivity r off of a perfect periodic multilayer for any situation.

Once we have r, the next step is to find a (set of) simpler material(s) whose reflectivity is exactly this complex number. Our first line of attack may involve just a single material with an unknown complex index of refraction $\tilde{n}$ as the substrate. In terms of the known parameters, this unknown index can be solved for uniquely:

$$\tilde{n}^2 = n_{Inc}^2 \left[\sin^2 q + \left(\frac{1-r}{1+r} \right)^2 \cos^2 q \right]. \tag{4}$$

While Eq. (4) provides what seems to be a simple solution to this problem, its inflexibility leads to potential danger. There are three types of problems that can occur. The first is the possibility that $\mathrm{Im}\,\tilde{n}$ can become negative and therefore completely unphysical. For small angles, it is easy to see that the sign of $\mathrm{Im}\,\tilde{n}$ is opposite to that of $\mathrm{Im}\,r$, so that when $\mathrm{Im}\,r > 0$, we must automatically rule out this single-material scheme. Secondly, even if $\mathrm{Im}\,\tilde{n}$ were positive, there is no guarantee that the resulting material improves the maximum allowed temporal step size. Aside from these two requirements, we must also verify that the

magnitude of the resulting value of $\tilde{n}$ is not too large, or else the spatial grid size may have to be brought down below a tolerable level to maintain an acceptable accuracy.

We therefore opt for a slightly more complicated scheme: a thin layer of material of unknown real index n_1 and thickness d sitting atop a substrate of index $\tilde{n}$. Now the substrate index $\tilde{n}$ takes a similar form to that in Eq. (4), but there is now a two-parameter family of solutions:

$$\tilde{n}^2 = n_{\text{Inc}}^2 \left[\sin^2 \boldsymbol{q} + \left(\frac{1 - \boldsymbol{r}'}{1 + \boldsymbol{r}'} \right)^2 \cos^2 \boldsymbol{q} \right], \tag{5}$$

where

$$\boldsymbol{r}' = \frac{(1 + \boldsymbol{r})\sqrt{n_1^2 - n_{\text{Inc}}^2 \sin^2 \boldsymbol{q}} - (1 - \boldsymbol{r})n_{\text{Inc}} \cos \boldsymbol{q}}{(1 + \boldsymbol{r})\sqrt{n_1^2 - n_{\text{Inc}}^2 \sin^2 \boldsymbol{q}} + (1 - \boldsymbol{r})n_{\text{Inc}} \cos \boldsymbol{q}} \exp\left[-i4\boldsymbol{p}\frac{d}{\boldsymbol{l}}\sqrt{n_1^2 - n_{\text{Inc}}^2 \sin^2 \boldsymbol{q}} \right], \tag{6}$$

and the quantities n_1 and d are to be varied until an "optimal" solution (in the sense described above) is found. This is the solution method we have chosen. A schematic of this substitution is illustrated in Figure 3.
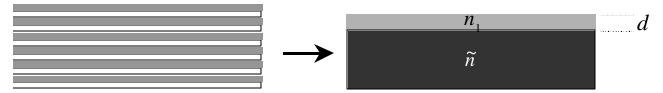

Figure 3. Illustrating the substitution of the multilayer on the left with the thin-film-on-substrate scheme on the right.

To illustrate how this procedure is to be implemented, we take the case of E-polarization using the parameters in Table 1. From the Appendix, we find the reflection coefficient $\boldsymbol{r} = 0.313995 - i\, 0.762709$. We then evaluate our figures of merit - that is, the maximum allowable time step and the corresponding value of $|\tilde{n}|$ - against n_1 and d. The range of these independent parameters is chosen with our goals in mind (e.g., we want n_1 to be in between, say, 1 and 2 for accuracy and stability purposes). We found many places in our search where the condition in Eq. (2) is satisfied and the Courant time step is valid. Whatever attractiveness this may have, however, is lost when we evaluate the corresponding value of $|\tilde{n}|$. We found that in the regions where the time step is a greatest, $|\tilde{n}|$ becomes large enough to cancel this benefit because of accuracy concerns.

It turns out that there is a fundamental tradeoff between Δt_{max}, the maximum allowed time step, and $|\tilde{n}|$, which points to how small a spatial step is required for a certain level of accuracy. The best we can do is to search the parameter space for that set which achieves a best compromise. Although we have no proof that this represents an optimal solution in any sense, we found an acceptable compromise in the values $n_1 = 1.10$ and $d = 7.5\,\text{nm}$, which gives us $\tilde{n} = 1.02905 + i\, 3.17568$. The corresponding value of $\Delta t_{\text{max}} = 0.059928\,\text{nm}$ here represents almost a factor of 6 improvement in speed over using the actual

multilayer materials in the grid. Another bonus is that we are also able to reduce the size of the simulation region in the *z*-direction, increasing the speed of the computation proportionally.

One last issue not explored here is the dependence of the reflectivity of the effective medium with angle. As small angles are used here, it can be assumed that the difference between this reflectivity and that for the multilayer is small. Nevertheless, we may have to fit several different angles at once in order to obtain sufficiently accurate results. In such a situation, one or more additional layers may need to be added in order to get the degrees of freedom necessary to speed the calculations as shown here.

4. Optimum Absorber Thickness

The above analysis only takes the multilayer substrate into account; it does not address the effect of the (chrome) absorber on top. It is clear that the substitution of materials as described above should have no effect on the on the reflectivity of the chrome. Even if the chrome thickness were small enough to let the radiation through, the reflectivity of the materials below – and not the actual composition of those materials – is all that matters.

This brings us to another question, however: what chrome thickness should we use? Ideally, the reflection coefficient off the chrome should be as close to zero as possible. We can perform a check on this by extending the analysis presented in the Appendix: simply front-multiply a matrix representing the chrome onto the multilayer system matrix. The results for E-polarization is presented in Figure 4, and are somewhat surprising in several respects. First, some past work spoke about simulation with chrome absorbers of thickness 50 nm. From these plots, it is clear that there is a non-negligible reflectivity off this chrome at this thickness. In fact, the magnitude of the electric field reflectivity here is about 0.165 in either polarization, and this may lead to some interference in the aerial image, as we will see below. Also, it is clear that there is a "sweet point" at a chrome thickness of about 83.2 nm, where the reflection coefficient almost vanishes. More importantly, this sweet point is almost the same in both polarizations (as one might expect for small angles). Nevertheless, its behavior with angle is a concern; we found that, although there was small enough variation at ± 2 degrees off the angle of incidence to not cause concern, larger angular ranges (corresponding to higher values of partial coherence) should be studied further.
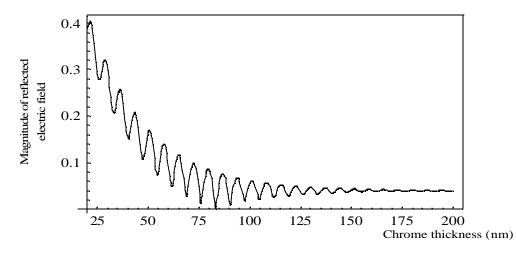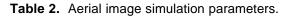

Figure 4. Plot of the magnitude of the complex reflectivity of chrome on multilayer as a function of chrome thickness. Note that the analogous plot for the substituted materials as described in the previous section is the same, as is the plot for H-polarization.

Given these results, the next question is to ask how such spurious reflections off the chrome can affect the aerial image. Furthermore, do we need an FDTD analysis to answer these questions thoroughly? To answer this, we must define our aerial image simulation parameters, and this is done in Table 2 below. The simulation procedure is as follows: We performed a rigorous mask topography simulation with ProMAX/2D. We then save the results of the reflected field just above the chrome and import the file into PROLITH/2 as a grayscale mask. Because the range of angles is so small, we will assume that the diffracted orders of the effective transmission function do not depend on angle (i.e., the Hopkins' approximation); this allows us to do a partially coherent simulation with one mask topography simulation.

Parameter	Symbol	Value
Partial Coherence	s	0.35
Numerical Aperture	NA	0.1
Reduction Ratio	R	5.0

Table 2. Aerial image simulation parameters.

Before performing the aerial image simulation, it is worthwhile to examine just the electric fields just that will be sent to the aerial image simulator. For these plots, only E-polarization was examined, although similar results are expected for H-polarization. In Figure 5, the magnitude of the fields corresponding to several chrome thicknesses (20, 50, 83.2, and 100 nm) are plotted together with what we will denote as the reflective Kirchhoff approximation: a piecewise constant function with transmission values equal to the complex reflectivity of the multilayer/chrome. As can be seen in this Figure, the major difference between the full FDTD simulations and the Kirchhoff approximation lies in the asymmetric spikes that are characteristic of oblique scattering from a corner. Note that the height of these spike rises with the chrome thickness. There also seems to be a small disparity in the value of the intensities in the spaces of these masks. There are two possible explanations of this. First, the effective medium may require a slightly lower spatial step size in order to achieve the necessary accuracy. Also, the small scattered fields off the chrome corners reflect off the effective material at different angles than for which the medium was designed, and such fields therefore may carry small errors from the slightly incorrect reflectivity.
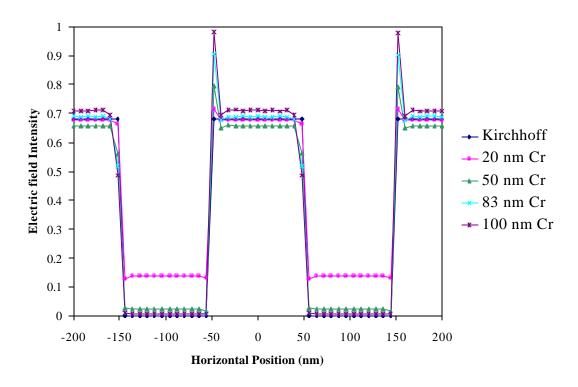
Figure 5. Plot of the reflected electric field intensity just above the chrome absorber for various chrome thicknesses. The small disparity in the intensities in the spaces is due to the difference in angular dependence between the electric field reflectivities of the actual multilayer and the effective medium.

What effect does this asymmetry have on the aerial image? In Figure 6, a comparison is made between the sweet point defined above and the Kirchhoff aerial images, and it is immediately obvious that the asymmetry in the electric field near the mask is translated into an asymmetry in the aerial image. [What seems to be a shifting of the image is not a simple translation from the oblique angle of incidence; that factor was taken out before the aerial image was computed.] While this asymmetry might seem mild, the use of smaller linewidths can exaggerate this effect greatly.

Figure 7 details the comparison between the various chrome thicknesses. Here, we simulated with thicknesses of 20, 50, 83.2, and 100 nm in order to study the effect of the spurious reflections from the chrome. It is clear that those masks with greater reflections off the chrome have larger sidelobes, and hence larger linewidths. Also, in Figure 8, the dependence of the aerial image intensity in the center of the chrome on defocus is shown for various chrome thicknesses. Here we can see how much work is left to be done: although the aerial images associated with the sweet point show less sensitivity to defocus than do other thicknesses, the overall dependence of all the thicknesses shown tend to increase too quickly on one side of focus, owing to the image asymmetry suffered here.
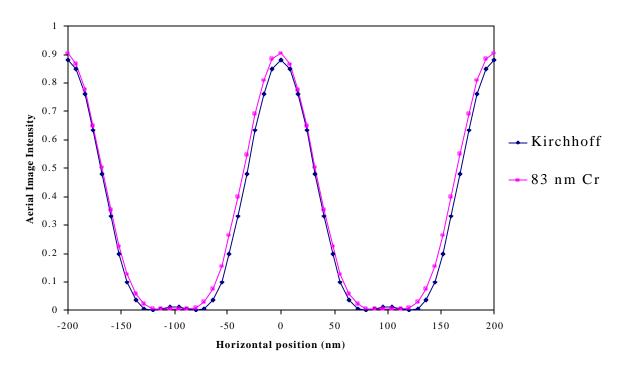
Figure 6. Comparison of the aerial image intensities of the "sweet" chrome thickness against the reflected Kirchhoff mask. The spike in the rigorous E-field causes an asymmetry in the aerial image that only gets worse with shrinking linewidths and increasing chrome thickness.
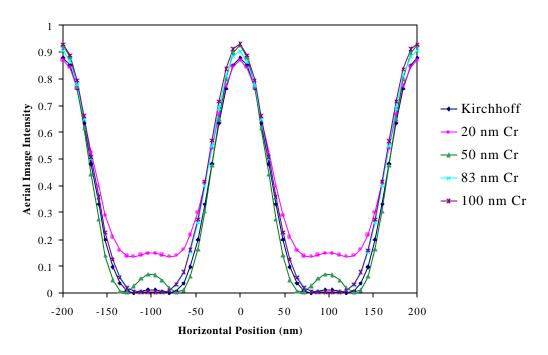

Figure 7. Comparison of the aerial images for various Chrome thicknesses. The sidelobes formed spurious reflections off the absorber has some consquences for the effective linewidth of the image.
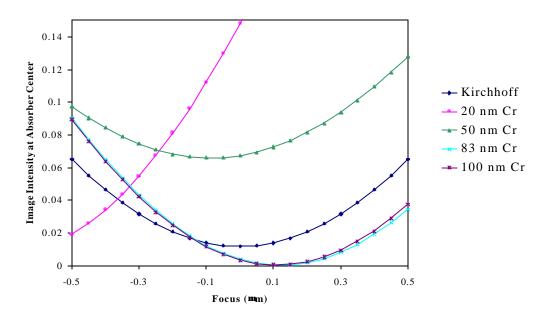
Figure 8. Dependence of image intensity at the absorber center with defocus for various chrome thicknesses. Again, the image asymmetry plays an important role here.

5. Concluding Remarks

The main result of this work is a paradigm for analyzing topography effects for EUV, or any reflective, masks. First, one determines the maximum spatial step and time step needed for a stable and accurate solution from the actual multilayer parameters. Then a reflectivity calculation is performed, and the result is used to determine a single thin-film scheme that significantly improves the maximum allowed time step and/or the maximum spatial step. The resulting parameters are fed into the mask topography simulator, and the reflected field just above the absorber is input to an aerial image simulator. These steps are outlined pictorially in Figure 9.
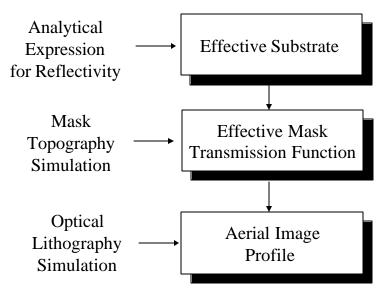

Figure 9. Diagram of methodology for computing rigorous aerial images in EUV lithography.

This work represents a first step in addressing EUV topography issues. One problem that was seen and not corrected here was that of image asymmetry due to the oblique incidence of the radiation. Pistor, *et al.*, found a way to reduce the intensity spike at the corner of the absorber through the use of small tapered feet at the bottom of the chrome sidewalls[3]. It is not clear, however, that this fix could work over even a moderate range of angles used in actual partially coherent sources. Obviously, more simulation work needs to be done here, and once a satisfactory conclusion is reached, it may become an important part of EUV mask design.

Of course, the analytical techniques outlined here provide other opportunities to facilitate EUV topography computation, as we have seen with the chrome-on-multilayer example here. Such calculations can be extended to any reasonable number of materials, either external or internal to the multilayer. Such calculations are crucial to the time savings-techniques applied here, in the form of the effective medium. Further study with regard to this topic is needed, however, in evaluating the difference in the angular dependence between the electric field reflectivities of the multilayer and the effective medium. This difference may generate small errors in the scattered field, and we therefore must explore more complicated schemes that provide a fit to the reflectivity over several angles.

Another idea not explored in detail is the design of a phase-shifting EUV mask. Although EUV imaging systems enjoy a large depth of focus due to the small NA employed, smaller linewidths will eventually be problematic with the conventional line/space setup currently employed. The task here will be much more challenging than that for transmissive masks[13], however. First, only whole periods can be subtracted from a space, lest the reflectivity of the resulting substrate be radically reduced. Also, the phase change comes not only from the extra path length in the phase-shifted region, but also from the change in reflectivity off the multilayer itself.

In the material substitution procedure outlined above, the original time step (the one corresponding to the original multilayer) was much smaller than that needed for the desired accuracy. This problem is common when dealing with a system of coupled differential equations, like those in Maxwell's equations. Such systems are known as "stiff" sets of differential equations when dealing with ordinary differential equations, but the concept is the same for our case: a solution with a large damping factor – a factor which should be negligible compared to the non-transient portion of the solution – causes an instability if the chosen stepsize is too large[14]. The solution proposed here is, in effect, an informal treatment of a stiff set of differential equations. The more formal treatments in the numerical literature are also worth exploring so that the runtime of these topography simulations are brought more in line with those for transmissive masks.

Appendix. Matrix formulation of reflectivity calculations.

The purpose of this Appendix is to derive and present formulae relating to the reflectivity of multilayer materials. This material is not new, and most of the following equations can be found readily in the literature[15]. The hope, however, is to remove some of the mystery surrounding these calculations and make them accessible to the lithography community.

The following calculations are detailed only for E-polarization (defined below). The results for H-polarization are analogous and only final results are presented.

We begin by considering a stack of $2N$ materials, each with (complex) refractive index n_j and thickness h_j. It is necessary to consider only the tangential components of the fields for this calculation. For E-polarization, this means we work with E_y and H_x, and we assume that these fields take the form of plane waves incident in vacuum upon the stack. Because we are only interested in the behavior of these fields along the direction of propagation, we strip off all other coordinate and time dependence:

$$E_y(x, z, t) = U(z) \exp\left[-i\frac{2p}{l}(xn\sin q + t)\right],$$ (A1)

$$H_x(x, z, t) = V(z) \exp\left[-i\frac{2p}{l}(xn\sin q + t)\right],$$ (A2)

where n is any material in the stack, and q is the corresponding angle of propagation within that material, and t is the time scaled to the speed of light in vacuum. [Note that the quantity $n\sin q$ is a constant throughout the stack.]

The two field quantities above are related through a component of Maxwell's equations:

$$\frac{\partial H_x}{\partial t} = \sqrt{\frac{e_0}{m_0}}\frac{\partial E_y}{\partial z},$$ (A3)

where the constants e_0 and m_0 refer to the permittivity and permeability of the vacuum, respectively. Eq. (A3) leads to the following relation between U and V:

$$V(z) = i\frac{l}{2p}\sqrt{\frac{e_0}{m_0}}\frac{dU(z)}{dz}.$$ (A4)

Because the fields satisfy Maxwell's equations, they also satisfy the wave equation. With the time factored out, the quantities U and V satisfy the following differential equations:

$$\frac{d^2U}{dz^2} + a^2U = 0,$$ (A5)

$$\frac{d^2V}{dz^2} + a^2V = 0,$$ (A6)

where $a = 2p\,n\cos q / l$. The solutions of both equations together involve 4 arbitrary constants; Eq. (A4), however, brings that number back to 2. Those 2 constants are then expressible in terms of the values of U and V at $z = 0$. We skip the details here; it turns out that these quantities are related to their initial conditions through a simple matrix multiplication. For this calculation, however, we wish to express the initial conditions in terms the fields. The result takes the form

$$\begin{pmatrix} U(0) \\ V(0) \end{pmatrix} = \begin{pmatrix} \cos a\,z & -\frac{i}{p}\sin a\,z \\ -ip\sin a\,z & \cos a\,z \end{pmatrix}\begin{pmatrix} U(z) \\ V(z) \end{pmatrix},$$ (A7)

where $p = \sqrt{(e_0/m_0)}\,n\cos q$ is analogous to the optical momentum of the system. (The minus signs in Eq. (A7) arises from the fact that the stack depth increases with negative z.) Note that the matrix in Eq. (A7) is unimodular – that is, it has unit determinant.

Eq. (A7) is crucial to this analysis, because it can be evaluated recursively. That is, the field at the bottom of one layer can be the incident field for the next layer. From this observation, one can then relate the field at the top of the stack to that at the bottom:

$$\begin{pmatrix} U(0) \\ V(0) \end{pmatrix} = \prod_{j=1}^{2N} \begin{pmatrix} \cos \boldsymbol{a}_j h_j & -\dfrac{i}{p_j} \sin \boldsymbol{a}_j h_j \\ -i p_j \sin \boldsymbol{a}_j h_j & \cos \boldsymbol{a}_j h_j \end{pmatrix} \begin{pmatrix} U(z_{2N}) \\ V(z_{2N}) \end{pmatrix},$$

(A8)

where z_{2N} is the position of the bottom of the stack. All of the information about the multilayer is contained in the matrix product above. This product can be written as a single matrix:

$$\begin{pmatrix} U(0) \\ V(0) \end{pmatrix} = \begin{pmatrix} m_{11} & m_{12} \\ m_{21} & m_{22} \end{pmatrix} \begin{pmatrix} U(z_{2N}) \\ V(z_{2N}) \end{pmatrix},$$

(A9)

and this net matrix is unimodular.

We can use the net system matrix in Eq. (A9) to evaluate the reflectivity of the multilayer stack. If the initial optical momentum of the radiation is p_0, and the momentum of the radiation in the substrate below the multilayer is p_b, then from Eq. (A4), it is straightforward to show that the complex reflectivity of the multilayer $\boldsymbol{r}$ takes the form

$$\boldsymbol{r} = \frac{(m_{11} + m_{12} p_b) p_0 - (m_{21} + m_{22} p_b)}{(m_{11} + m_{12} p_b) p_0 - (m_{21} + m_{22} p_b)}.$$

(A10)

Eq. (A10) is valid for any number of materials of any complex index. In general, there are no simple, analytical expressions for the matrix elements. On the other hand, for the special case of a periodic multilayer – which is the situation in EUV lithography – there are closed form expressions. These expressions follow from the fact that the Nth power of a unimodular 2X2 matrix $\mathbf{M}$ with elements m_{ij} is given by

$$\mathbf{M}^N = \begin{pmatrix} b_{11} & b_{12} \\ b_{21} & b_{22} \end{pmatrix},$$

(A11)

$$\begin{aligned} b_{11} &= m_{11} U_{N-1}(a) - U_{N-2}(a), \\ b_{12} &= m_{12} U_{N-1}(a), \\ b_{21} &= m_{21} U_{N-1}(a), \\ b_{22} &= m_{22} U_{N-1}(a) - U_{N-2}(a), \end{aligned}$$

(A12)

where $a = (m_{11} + m_{22})/2$, and the U_n are the Chebyshev polynomials of the 2$^{\text{nd}}$ kind[16]:

$$U_n(\cos \boldsymbol{J}) = \frac{\sin[(n+1)\boldsymbol{J}]}{\sin \boldsymbol{J}}.$$

(A13)

To compute the reflectivity of a periodic multilayer, then, one simply multiplies the system matrices for all of the materials in a period. Because the resulting matrix is unimodular, Eq. (A11) applies, and the

resulting matrix elements are used to evaluate the right-hand side of Eq. (A10). To include the effect of the absorber, one simply front-multiplies the multilayer system matrix by the absorber matrix and then uses the resulting matrix elements in Eq. (A10).

All of the above results apply to H-polarization, except that one replaces all the optical momenta p_j with $q_j = \sqrt{(\mu_0 / \varepsilon_0)} \cos \theta_j / n_j$.

References

[1] G.E. Sommargren and L.G. Seppala, "Condenser optics, partial coherence, and imaging for soft x-ray projection lithography", *Applied Optics* **32**, 6938-6944 (1993).

[2] K.B. Nguyen, A.K. Wong, A.R. Neurether, and D.T. Attwood, "Effects of absorber topography and multilayer coating defects on refletive masks for soft x-ray/EUV projection lithography", *Proc. SPIE vol. 1924, Electron Beam, X-Ray, and Ion Beam Submicrometer Lithographies for Manufacturing III,* D.O. Patterson, Ed., 418-434 (1993).

[3] T.V. Pistor, K. Adam, and A. Neurether, "Rigorous simulation of mask corner effects in extreme ultraviolet lithography", *J. Vac. Sci. Tech. B* **16**, 3449-3455 (1998).

[4] B.S. Bollepalli, M. Khan, and F. Cerrina, "Imaging properties of the extreme ultraviolet mask", *J. Vac. Sci. Tech. B* **16**, 344-3448 (1998).

[5] R.L. Gordon, C.A. Mack, "Lithography simulation employing rigorous solutions to Maxwell's equations", *Proc. SPIE, vol. 3334, Optical Microlithography XI*, L. Van den hove, Ed., 176-196 (1998).

[6] D.M. Tennant, L.A. Fetter, L.R. Harriott, A.A. MacDowell, P.P. Mulgrew, J.Z. Pastalan, W.K. Waskiewicz, D.L. Windt, and O.R. Wood II, "Mask technologies for soft x-ray projection lithography at 13 nm", *Applied Optics* **32**, 7007-7011 (1993).

[7] The indices of refraction for the materials in this table were taken from the excellent web site http://www-cxro.lbl.gov/optical constants/ , managed by E.M. Gullikson.

[8] W.H. Press, S.A. Teukolsky, W.T. Vetterling, and B.P. Flannery, "Numerical Recipes in C: The Art of Scientific Computing", 2nd Ed.. Cambridge: Cambridge University Press (1992), Sec. 19.1.

[9] P. Morse and H. Feshbach, *Methods of Theoretical Physics*. New York: McGraw-Hill (1953), p.706.

[10] R.L. Gordon, "Robust finite-difference, time-domain algorithm for solving Maxwell's equations in highly conductive media", to be submitted to *J. Opt. Soc. Am. A*.

[11] A.K. Wong, "Rigorous Three-Dimensional Time-Domain Finite-Difference Electromagnetic Smulation", Ph.D. Thesis, Memorandum N0. UCB/ERL M94/69, U. Cal., Berkeley (1994), Ch. 5.

[12] C.A. Mack, "Analytical expression for the standing wave intensity in photoresist", *Appl. Opt.* **25**, 1958-1961 (1986).

[13] R.L. Gordon, C.A. Mack, J.S. Petersen, "Design and analysis of manufacturable phase-shifting masks", in *18th Annual BACUS Symposium on Photomask Technology and Management*, B.J. Grenon, F.E. Abboud, Eds., Proc. SPIE Vol. 3546, 606-616 (1998).

[14] Ref. 8, pp. 734-736.

[15] This analysis follows that presented in M. Born and E. Wolf, *Principles of Optics*, 6th. Ed.. Oxford: Pergamon Press (1980). Secs. 1.6.1, 1.6.2, 1.6.3, 1.6.5, 13.4.

[16] Further properties of this function can be found in M. Abromawitz and I. Stegun, *Handbook of Mathematical Functions*, New York: Dover (1964), Ch. 22.